Intermetallics 52 (2014) 20–31

Contents lists available at ScienceDirect

Intermetallics

journal homepage: www.elsevier.com/locate/intermet

Dislocation slip and twinning in Ni-based $L1_2$ type alloys

J. Wang, H. Sehitoglu*

Department of Mechanical Science and Engineering, University of Illinois at Urbana-Champaign, 1206 W. Green St., Urbana, IL 61801, USA

ARTICLE INFO

Article history:
Received 3 October 2013
Accepted 18 March 2014
Available online

Keywords:
A. Nickel aluminides, based on Ni_3Al
A. Ternary alloy systems
D. Defects: dislocation geometry and arrangement
D. Defects: planar faults
E. Ab-initio calculations

ABSTRACT

We report theoretical results on dislocation slip and twinning in Ni_3 (Al, Ti, Ta, Hf) compositions with $L1_2$ crystal structures utilizing first-principles simulations. The lattice parameters of Ni_3Al, $Ni_3Al_{0.75}Ta_{0.25}$, $Ni_3Al_{0.5}Ta_{0.5}$, Ni_3Ta, Ni_3Ti and $Ni_3Al_{0.75}Hf_{0.25}$ are calculated, and the crystal structures with lower structural energies are determined. We established the Generalized Stacking Fault Energy (GSFE) and Generalized Planar Fault Energy (GPFE), and calculated stacking fault energies APB (anti-phase boundary) and CSF (complex stacking fault) matched other calculations and experiments. Based on the extended Peierls–Nabarro model for slip and the proposed twin nucleation model, we predict slip and twinning stress and the results show a general agreement with available experimental data. The results show that in the studied intermetallic alloys, twinning stress is lower than slip stress; Ta and Hf ternary addition are substantial to increase flow stress in Ni_3Al. The models proposed in the paper provide quantitative understanding and guidelines for selecting optimal precipitate chemistry and composition to obtain higher mechanical strength in Shape Memory Alloys.

1. Introduction

The quest for the theoretical determination of the stress required for plastic flow via slip and via twinning has been ongoing for many years and has become more important with the need for developing advanced materials [1–9]. Formulas for the stress required for dislocation motion (the slip stress) and the stress required for twin nucleation (the twin stress) have been proposed in our previous research combining atomistic simulations with mesoscale dislocation theory [10,11]. The former calculations rely on the well-known Peierls–Nabarro (P–N) description of the dislocation core, and the more recent calculations extend the P–N model to describe the twin [10]. These theoretical estimates have provided extremely close values compared to experiments in a number of B2 alloys [11]. The twinning mechanism can play an important role in crystals with limited number of independent slip systems, and may readily occur in experiments when the twinning stress magnitude is below the slip stress [10,12–15]. The present paper is on the application of these theories, with modifications to twinning modeling, to several $L1_2$ crystals that are of interest in shape memory alloys (SMAs).

Coherent, nontransforming precipitates in advanced SMAs proposed recently with unprecedented properties [16–20] have $L1_2$ crystal structures. These precipitates which are Ni-based can occupy a large volume fraction within the austenite or martensite domains. While they do not transform, they influence the transformation characteristics. These coherent precipitates exhibit superior flow resistance compared to the matrix but deform during the transformation to maintain compatibility. The benefit of the precipitates is that they can elevate the slip resistance of the matrix which imparts reversibility and shape memory to the alloy [19,21]. However, no quantitative model has been proposed for the assessment of deformation resistance of these precipitate phases. Many precipitate compositions are possible; in this paper, we specifically focus on the most important ones, the Ni_3 (Al, Ti, Ta) compositions with $L1_2$ crystal structures. It is not known a priory the relative magnitudes of slip and twinning stress for Ni_3 (Al, Ti, Ta) compositions. As mentioned above, the formulation presented in this paper utilizes an extended Peierls–Nabarro framework for slip and twinning utilizing atomistic simulations.

The role of fine precipitates on the shape memory response has been discussed originally by Hornbogen [22] and then by Koval and co-workers [23]. Although the mechanical behavior of the precipitates is not fully understood, they impart beneficial properties as discussed above. The recently proposed SMAs of the Fe variety undergo face centered cubic (fcc) to tetragonal crystal transformations where both the austenite and martensite phases are disordered [19,21,24]. The presence of coherent precipitates has been proposed to impart surprising thermoelastic shape

* Corresponding author. Tel.: +1 2173334112.
E-mail address: huseyin@illinois.edu (H. Sehitoglu).

http://dx.doi.org/10.1016/j.intermet.2014.03.009
0966-9795/

memory response in these alloys. The details of the shape memory response is outside the scope of this paper, but the modification of mechanical properties due to Ta and Hf additions on strengthening of these precipitates is within the scope of our investigation.

Recent studies of electronic structure calculations have developed an accurate description of the fault energy curves in metallic alloys. Different crystal structures, slip and twin planes and directions have been simulated. The original calculations have focused on the determination of ideal stresses [9], and more recently utilizing dislocation mechanics at the mesoscale a better estimation of flow resistance in agreement with experiments have been achieved [10,11]. Recent developments incorporated a better description of the dislocation core particularly for the case of fractional or partial dislocations. The results show excellent agreement with experiments for twinning [10] and slip [11] in a number of intermetallic alloys.

In this paper, we present the modeling efforts for slip and twinning for Ni_3 (Al, Ti, Ta, Hf) compositions with $L1_2$ crystal structures. The lattice parameters are studied as well as the crystal structure for the ground state by comparing $L1_2$ and other crystal structures. The modeling efforts require shear moduli and accurate description of GSFE and GPFE curves with internal relaxation. The GSFE curves represent the Generalized Stacking Fault Energy which is an accurate description of slip in the case of partial or full dislocation slip [25]. The GPFE curves represent the energy landscape associated with partial dislocations and describe the layer by layer growth of the twin [26]. Because the path leading to the twin formation deviates from that of slip, the GPFE and GSFE curves, hence the corresponding stress levels for the two mechanisms are not the same. We discuss this in detail for the materials of interest in this study.

2. Simulation methods

We utilized Density Functional Theory (DFT) to investigate the crystal structure energy and establish GSFE and GPFE curves. The first-principles total-energy calculations were carried out using the Vienna *ab initio* Simulations Package (VASP) [27,28] with the projector augmented wave (PAW) method and the generalized gradient approximation (GGA). In our calculations, Monkhorst–Pack $9 \times 9 \times 9$ *k*-point meshes were used for the Brillouin-zone integration. Ionic relaxation was performed by a conjugate gradient algorithm and stopped when absolute values of internal forces were smaller than 5×10^{-3} eV/Å. The energy cut-off of 500 eV was used for the plane-wave basis set. The total energy was converged to less than 10^{-5} eV per atom. We have used an *n*-layer based cell to calculate fault energies to generate GSFE and GPFE curves for studied materials. We assessed the convergence of the GSFE and GPFE energies with respect to increasing *n*, which indicates that the fault energy interaction in adjacent cells due to periodic boundary conditions will be negligible. The convergence is ensured once the energy calculations for n and $n+1$ layers yield the same GSFE and GPFE. In the present study, we performed a full atomic relaxation to establish the GSFE and GPFE. During full relaxation the atoms can move in the out of plane and normal to the slip and twin plane although these displacements are small relative to the shear displacement. This relaxation process caused a small additional atomic displacement r $\left(|r| = \sqrt{r_x{}^2 + r_y{}^2 + r_z{}^2}\right)$ deviating from the Burgers vector. Thus, the total fault displacement is not exactly equal to u but involves additional r. The total energy of the deformed (faulted) crystal was minimized during this relaxation process through which atoms can avoid coming too close to each other during shear [29–31].

3. Results and discussion

We studied several Ni-based $L1_2$ type binary and ternary alloys: Ni_3Al, $Ni_3Al_{0.5}Ta_{0.5}$, $Ni_3Al_{0.75}Ta_{0.25}$, Ni_3Ta, Ni_3Ti and $Ni_3Al_{0.75}Hf_{0.25}$. We note that theoretical studies of $L1_2$ Ni_3Al (crystal structure, dislocation slip and twin) can be found in literature [32–39]. Ni_3Ta and Ni_3Ti having the $L1_2$ crystal structure are similar to Ni_3Al, and thus, in this paper we will only report the results in Tables 1 and 2 without giving calculation details for these three materials. Instead, the ternary alloys $Ni_3Al_{0.5}Ta_{0.5}$ and $Ni_3Al_{0.75}Ta_{0.25}$ will be focused in the paper including the determination of crystal structure, prediction of dislocation slip and twin nucleation stress (Section 3.1). Since the atomic arrangements of $Ni_3Al_{0.75}Hf_{0.25}$ are similar to those of $Ni_3Al_{0.75}Ta_{0.25}$, we will only report the calculated results for this material in Tables 1 and 2.

We plot the predicted dislocation slip and twinning stress of the Ni-based $L1_2$ type alloys variation with the composition x in Fig. 1. The composition x can be considered as the concentration of R in $Ni_3Al_{(1-x)}R_x$ for R = Ta, Hf and Ti. We note that for all these alloys, the twinning stress (circle) is lower than slip stress (square), which indicates that twinning is more favorable than dislocation slip as the deformation mechanism. Twinning is experimentally observed and theoretically found in $L1_2$ alloys as a significant deformation mechanism [32,40–44]. Although the values of slip stress are higher than those of twinning, the difference is not significant and the dislocation slip can be activated due to the sufficiently high local stress. Thus, dislocation slip is also often observed experimentally in $L1_2$ alloys [45–50]. For the alloy $Ni_3Al_{(1-x)}Ta_x$ in Fig. 1, we note that both slip and twinning stress increase as composition x becomes larger, but after $x = 0.5$, they are increasing slowly and reach maximum values at $x = 1$. In addition, by comparing the Ni_3Ti and Ni_3Ta, we note that the values of slip and twinning stress in Ni_3Ta are higher than Ni_3Ti by around 9%, so Ta should be more suitable than Ti for obtaining high mechanical strength in SMAs. Furthermore, we note that the values of slip and twinning stress in $Ni_3Al_{0.75}Hf_{0.25}$ are higher than $Ni_3Al_{0.75}Ta_{0.25}$ by around 15%, and very close to those of $Ni_3Al_{0.5}Ta_{0.5}$. This indicates that the addition of Hf should be more efficient than other chemistries to increase the deformation resistance in SMAs.

3.1. $Ni_3Al_{0.5}Ta_{0.5}$

3.1.1. Crystal structure in $Ni_3Al_{0.5}Ta_{0.5}$

In order to study the crystal structure of $Ni_3Al_{0.5}Ta_{0.5}$ (atomic ratio is 6:1:1), two different supercells termed '$L1_2$-like' and '$D0_{22}$-like' are constructed [61]. Both these supercells consist of two $L1_2$ subcells with total eight atoms [61,62]. The $L1_2$-like supercell (Fig. 2a) can be constructed from a supercell containing two $L1_2$ Ni_3Al subcells, but the Al occupying the middle corners of the supercell and shared by the two subcells, are replaced by Ta. Since there are six Ni at the face centers in each subcell (three Ni atoms), altogether there are six Ni atoms in the $L1_2$-like supercell. In addition, eight Al occupy the top and bottom corners and four Ta

Table 1
Calculated lattice parameter and Burgers vector are compared to other calculations and experimental data in Ni-based $L1_2$ type alloys.

Materials ($L1_2$)	Lattice parameter (Å)		Burgers vector (Å)
	This study	Experiments	This study
Ni_3Al	3.58	3.57 [45,51], 3.58 [52]	1.46
$Ni_3Al_{0.75}Ta_{0.25}$	3.60	3.61 [53]	1.47
$Ni_3Al_{0.5}Ta_{0.5}$	3.62	3.625 [53,54]	1.48
Ni_3Ta	3.68	3.69 [53]	1.50
Ni_3Ti	3.62	3.62 [55]	1.48
$Ni_3Al_{0.75}Hf_{0.25}$	3.62	3.615 [53]	1.48

Table 2
Calculated energy associated to dislocation slip (GSFE) and twin (GPFE), slip and twinning stress are compared to other calculations and experimental data in Ni-based $L1_2$ type alloys.

Materials ($L1_2$)	GSFE (slip) (mJ/m^2)						GPFE (twin) (mJ/m^2)		Slip stress (MPa)		Twinning stress (MPa)
	γ_{s1}	γ_{s2}	CSF		APB		γ_{ut}	$2\gamma_{tsf}$	This study	Experiments	This study
			This study	Other calculations/ experiments	This study	Other calculations/ experiments					
Ni_3Al	276	682	241	236 [56] 250 [37]	223	195 [56] 237 [37]	432	169	164	150 [45] 130 [46] 83 [57]	148
$Ni_3Al_{0.75}Ta_{0.25}$	873	1134	552	396 [58]	615	610 [59]	976	554	517	450 [48]	395
$Ni_3Al_{0.5}Ta_{0.5}$	635	1331	320	599 [60]	505	443 [59] 476 [60]	1040	500	603	–	490
Ni_3Ta	330	856	−300	−450 [60]	−577	−500 [59] −691 [60]	628	279	622	–	536
Ni_3Ti	627	1378	460	468 [60]	516	550 [58] 540 [59]	1065	244	578	450–834 [47]	495
$Ni_3Al_{0.75}Hf_{0.25}$	902	1177	612	–	734	–	1007	607	588	–	456

The dash indicates that experimental data were not available for comparison.

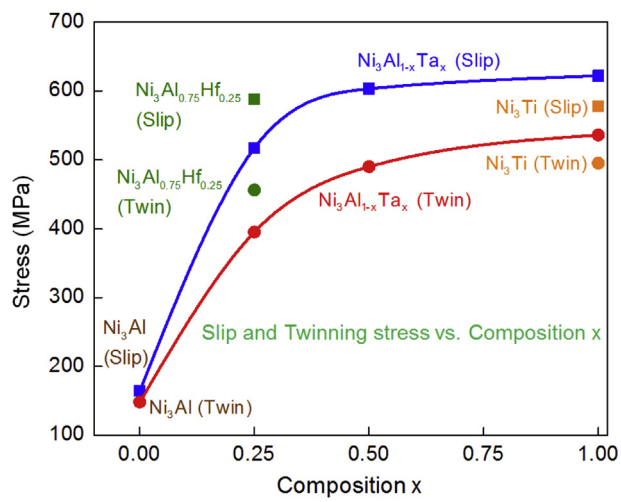

Fig. 1. Predicted dislocation slip and twinning stress of the Ni-based $L1_2$ type alloys, $Ni_3Al_{(1-x)}R_x$ for R = Ta, Hf and Ti, variation with composition *x*. The stress values are shown in Table 2.

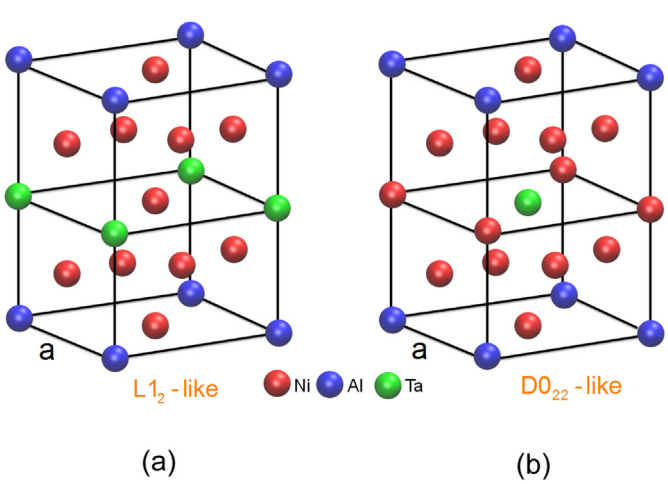

Fig. 2. Two crystal structures of $Ni_3Al_{0.5}Ta_{0.5}$ (a) $L1_2$-like structure and (b) $D0_{22}$-like structure. There are total eight atoms in each structure and the atomic ratio is 6:1:1.

occupy the middle corners, so there is total one Al atom and one Ta atom. Therefore, in the supercell the atomic ratio is 6:1:1. The $D0_{22}$-like supercell (Fig. 2b) is similar to the $L1_2$-like supercell and possesses the atomic ratio of 6:1:1. The difference between these two supercells is that the Ta in the $D0_{22}$-like supercell is at the body center (occupy Ni sites) instead of being at the middle corners (occupy Al sites) in the $L1_2$-like supercell.

To determine the stability of the two different structures for $Ni_3Al_{0.5}Ta_{0.5}$, we calculated total energy as a function of lattice parameter of the $D0_{22}$-like structure and the $L1_2$-like structure shown in Fig. 3. We note that $Ni_3Al_{0.5}Ta_{0.5}$ in the $L1_2$-like structure is energetically favored over the $D0_{22}$-like structure, because in the entire rage of lattice parameters the total energies of the $L1_2$-like structure are lower than those of the $D0_{22}$-like structure by near 0.2 eV per formula unit. These results indicate that when we consider the $Ni_3Al_{0.5}Ta_{0.5}$ as the ternary additions of Ta in Ni_3Al, the Ta will preferentially occupy the Al sites ($L1_2$-like structure) over than the Ni sites ($D0_{22}$-like structure). Our calculations are consistent with $Ni_3Al_{0.5}V_{0.5}$ [61] and $Ni_3Al_{0.5}Nb_{0.5}$ [63], where the $L1_2$-like structure is more stable than other structures in these two materials. Therefore, in the following studies of dislocation slip and

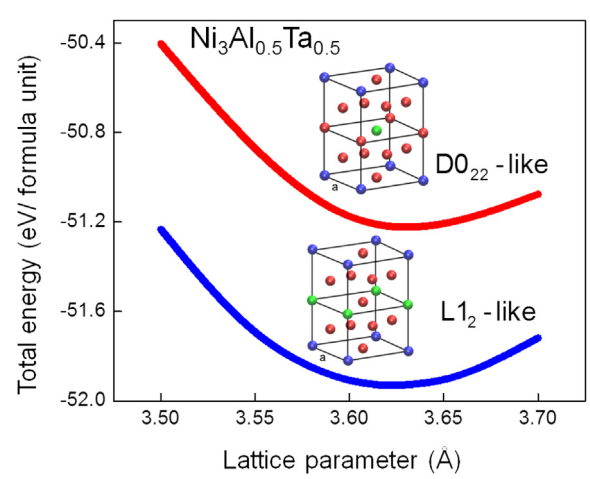

Fig. 3. Total energy as a function of lattice parameter for $D0_{22}$-like (read line) and $L1_2$-like (blue line) $Ni_3Al_{0.5}Ta_{0.5}$. The total energies of the $L1_2$-like structure are lower than those of the $D0_{22}$-like structure by near 0.2 eV per formula unit. The calculated lattice parameter is compared to other calculations and experiments shown in Table 1. (For interpretation of the references to color in this figure legend, the reader is referred to the web version of this article.)

twin nucleation in $Ni_3Al_{0.5}Ta_{0.5}$, we established the GSFE and GPFE curves for $L1_2$-like structure as it has greater stability.

3.1.2. Dislocation slip (GSFE) in $L1_2$-like $Ni_3Al_{0.5}Ta_{0.5}$

In this study, we investigate the slip system {111}<110> for $Ni_3Al_{0.5}Ta_{0.5}$, which is often experimentally observed in $L1_2$ crystal structure [34,36,64,65]. The <110> superdislocation in the {111} slip plane can dissociate into two 1/2<110> superpartials with formation of APB (anti-phase boundary) energy. The superpartial can further dissociate into two Shockely partials 1/6<112> connected by CSF (complex stacking fault) energy [32,35,66–68]. This process results in a fourfold dissociation in Eq. (1):

$$\left[\bar{1}10\right] = \frac{1}{6}\left[\bar{2}11\right] + \mathrm{CSF} + \frac{1}{6}\left[\bar{1}2\bar{1}\right] + \mathrm{APB} + \frac{1}{6}\left[\bar{2}11\right] + \mathrm{CSF} + \frac{1}{6}\left[\bar{1}2\bar{1}\right] \quad (1)$$

Fig. 4 shows a top view from the direction perpendicular to the (111) slip plane with three-layer of atoms stacking in $Ni_3Al_{0.5}Ta_{0.5}$. Three different sizes of atoms indicate three successive (111) layers from the top view, which is similar to fcc metals. However, certain symmetries existing in fcc lattice are not found in $L1_2$ lattice. We note that {110} planes composed of only Ni atoms (shown in brown dashed line in Fig. 4) are not planes of mirror-symmetry in the $L1_2$ lattice, which is different with the case of fcc lattice where every {110} plane has this symmetry [69]. Therefore, the superdislocation $[\bar{1}10]$ (brown arrow) in $L1_2$ lattice must dissociate into four superpartials 1/6<211> (blue arrow) corresponding to Eq. (1). While in fcc lattice, the full dislocation $1/2[\bar{1}10]$ dissociates into two partials 1/6<211> [35,70]. Two types of planar defects CSF and APB are formed

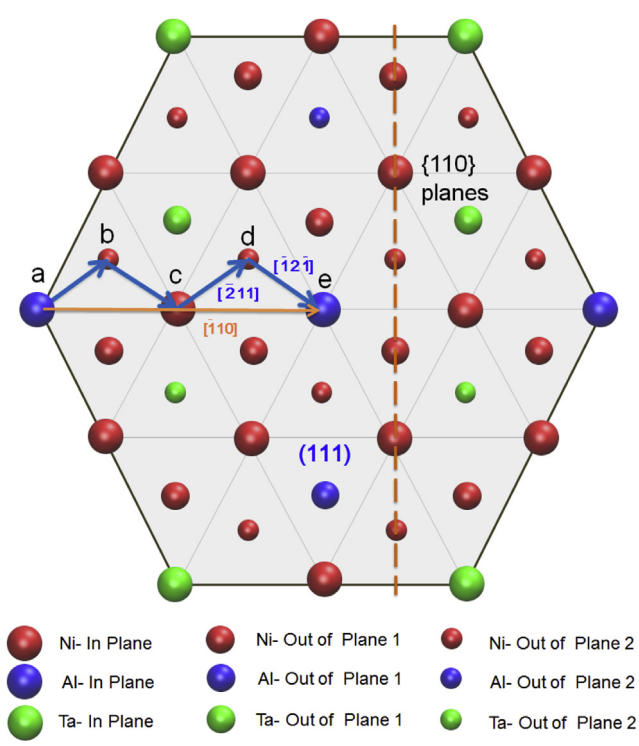

Fig. 4. Dislocations and atomic configuration of $L1_2$-like $Ni_3Al_{0.5}Ta_{0.5}$ in the (111) plane. Three different sizes of atoms represent three successive (111) layers from the top view. Dislocation $[\bar{1}10]$ can dissociate into four superpartials 1/6<211> corresponding to Eq. (1). Two types of planar defects CSF (a → b and c → d) and APB (a → c and c → e) are formed. The points a, b, c, d and e correspond to the stable (metastable) positions in GSFE curve described later. The {110} planes composed of only Ni atoms (shown in brown dashed line) are not planes of mirror-symmetry in the $L1_2$ lattice. (For interpretation of the references to color in this figure legend, the reader is referred to the web version of this article.)

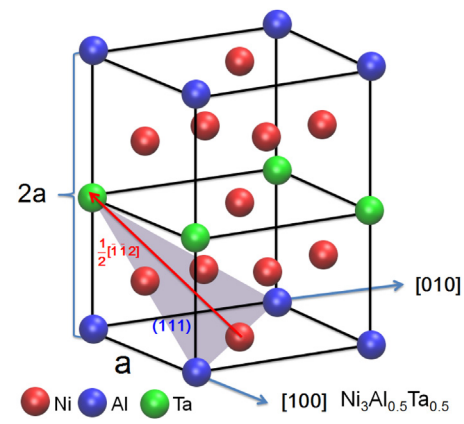

Fig. 5. Slip plane (111) (shaded violet) and slip direction $[\bar{1}\,\bar{1}2]$ (red arrow) in $L1_2$-like $Ni_3Al_{0.5}Ta_{0.5}$. The $L1_2$-like supercell consists of two $L1_2$ subcells with total eight atoms. (For interpretation of the references to color in this figure legend, the reader is referred to the web version of this article.)

with the dissociation of superdislocation $[\bar{1}10]$ in $L1_2$, which does not exhibit in fcc metals. A CSF is produced when the in-plane atoms and all atoms above are shifted along the Burgers vector $1/6[\bar{2}11]$ (a → b and c → d in Fig. 4). An APB is formed when the in-plane atoms and all atoms above are shifted along the Burgers vector $1/2[\bar{1}10]$ (a → c and c → e in Fig. 4). The points a, b, c, d and e correspond to the stable (metastable) positions in the GSFE curve described later.

Fig. 5 shows the slip plane (111) (shaded violet) and slip direction $\left[\bar{1}\,\bar{1}2\right]$ (red arrow) in $L1_2$-like $Ni_3Al_{0.5}Ta_{0.5}$. The lattice parameter a is calculated as 3.62 Å in Fig. 3, which is in a good agreement with experimental measurements (Table 1).

The slip energy barriers (unstable stacking fault energies) and planar defect energies (CSF and APB) are all characterized by the GSFE curve, which is calculated when one half crystal is shifted relative to the other in the slip plane along the slip direction [12]. The $1/6\left[\bar{1}\,\bar{1}2\right](111)$ case of $L1_2$-like $Ni_3Al_{0.5}Ta_{0.5}$ is illustrated in Fig. 6 showing the configuration of slip in the plane (111) with dislocation $1/6\left[\bar{1}\,\bar{1}2\right]$. Fig. 6a is the perfect $L1_2$ lattice before shear, while Fig. 6b is the lattice after shear by one Burgers vector, $b = \sqrt{6}/6a = 1.48$Å, in the slip plane. All fault energies can be computed as a function of shear displacement, u, and are determined relative to the energy of the undeformed $L1_2$.

The calculated GSFE curve in the slip system 1/6<112>(111) is shown in Fig. 7. The points a, b, c, d and e correspond to the stable (metastable) positions in the GSFE curve (see atomic configuration in Fig. 4). The calculated stacking fault energies are compared well to other calculations and experimental data in Table 2. The Peierls stress of $L1_2$-like $Ni_3Al_{0.5}Ta_{0.5}$ is calculated as 603 MPa (Table 2) utilizing our extended Peierls–Nabarro model described in Appendix A.

3.1.3. Twin nucleation (GPFE) in $L1_2$-like $Ni_3Al_{0.5}Ta_{0.5}$

We calculated the GPFE curve of the $L1_2$-like $Ni_3Al_{0.5}Ta_{0.5}$ by successive shear of every (111) plane over $1/6[\bar{1}\bar{1}2]$ twinning partial (the twinning Burgers vector $b = \sqrt{6}/6a = 1.48$Å) [10,12]. Fig. 8a shows the perfect lattice of $L1_2$-like $Ni_3Al_{0.5}Ta_{0.5}$, while Fig. 8b is the lattice with a three-layer twin after shearing 3b (shown in a red arrow) in successive (111) planes (twin plane is marked with a brown dashed line). The atomic arrangement is viewed from the $[\bar{1}10]$ direction.

The calculated energy landscape (GPFE) for a three-layer twin formation in $L1_2$-like $Ni_3Al_{0.5}Ta_{0.5}$ is shown in Fig. 9. The calculated energies associated to the twin process are shown in Table 2. The critical twin nucleation stress of $L1_2$-like $Ni_3Al_{0.5}Ta_{0.5}$ is calculated

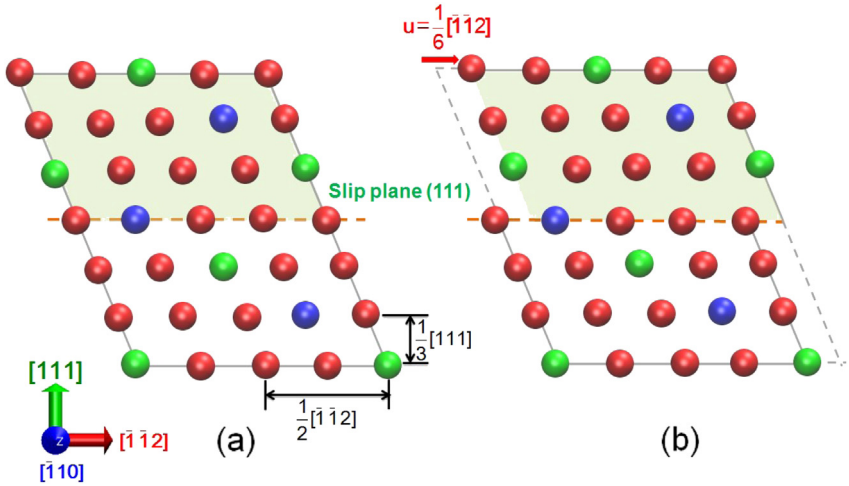

Fig. 6. Dislocation slip in the (111) plane with dislocation $1/6[\bar{1}\,\bar{1}2]$ of $L1_2$-like $Ni_3Al_{0.5}Ta_{0.5}$. (a) The perfect $L1_2$-like lattice observed from the $[\bar{1}10]$ direction. The slip plane (111) is marked with a brown dashed line. (b) The lattice after a rigid shear with dislocation $1/6[\bar{1}\,\bar{1}2]$, u, shown in a red arrow. (For interpretation of the references to color in this figure legend, the reader is referred to the web version of this article.)

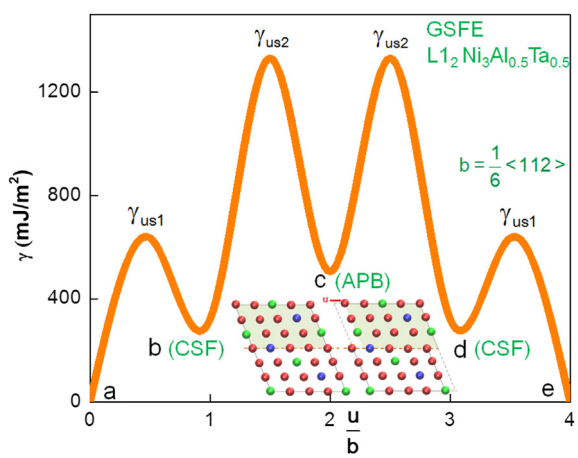

Fig. 7. The GSFE curve of the slip system 1/6<112>(111) in $L1_2$-like $Ni_3Al_{0.5}Ta_{0.5}$. The dislocation $[\bar{1}10]$ can dissociate into four superpartials 1/6<112> connected by stacking fault energies CSF and APB. The calculated CSF, APB and unstable stacking fault energies are shown in Table 2. The points a, b, c, d and e correspond to the stable (metastable) positions in the GSFE curve (see atomic configuration in Fig. 4).

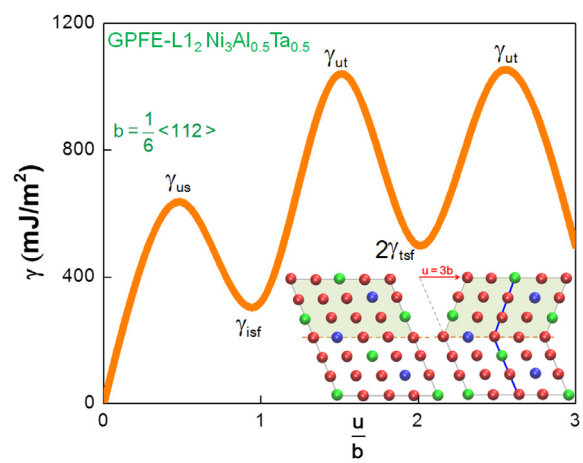

Fig. 9. The GPFE curve in the twin plane (111) with twin dislocation $1/6[\bar{1}\bar{1}2]$ of $L1_2$-like $Ni_3Al_{0.5}Ta_{0.5}$. The shear displacement, u, is normalized by the twinning Burgers vector $b = 1/6[\bar{1}\bar{1}2]$. The calculated fault energies are shown in Table 2.

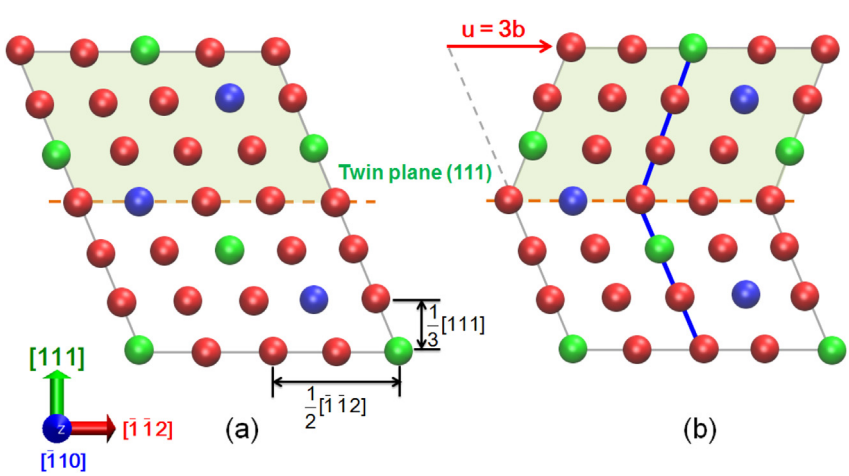

Fig. 8. (a) The perfect $L1_2$-like lattice viewed from the $[\bar{1}10]$ direction. Twin plane (111) is marked with a brown dashed line. (b) The lattice with a three-layer twin after shearing 3b along $1/6[\bar{1}\,\bar{1}2]$ shown in a red arrow. (For interpretation of the references to color in this figure legend, the reader is referred to the web version of this article.)

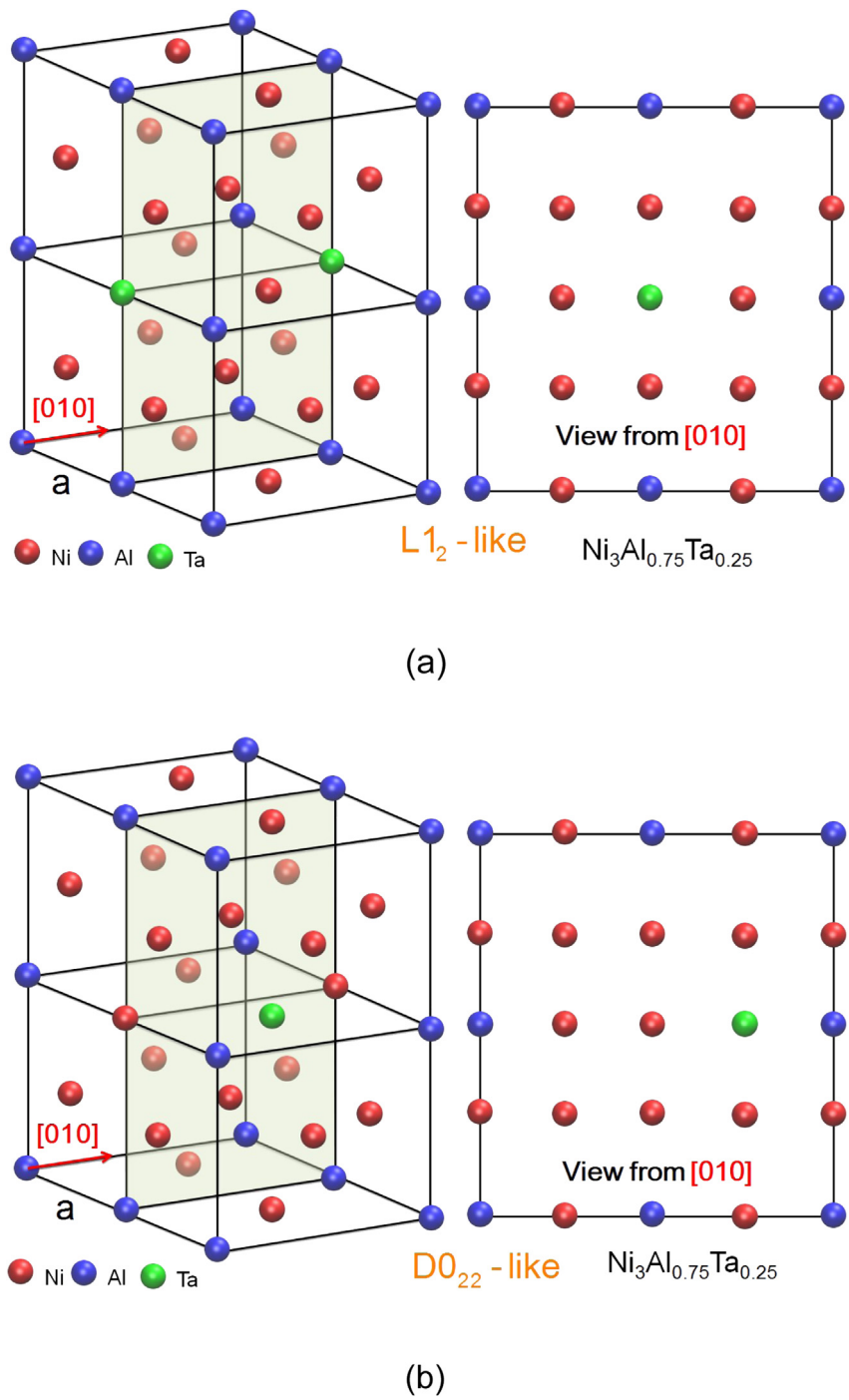

Fig. 10. Two crystal structures of $Ni_3Al_{0.75}Ta_{0.25}$ (a) $L1_2$-like structure and the view from [010] direction. (b) $D0_{22}$-like structure and the view from [010] direction.

as 490 MPa (Table 2) utilizing our developed twin nucleation model described in Appendix B.

3.2. $Ni_3Al_{0.75}Ta_{0.25}$

3.2.1. Crystal structure in $Ni_3Al_{0.75}Ta_{0.25}$

Similar to the case of $Ni_3Al_{0.5}Ta_{0.5}$, we constructed two different supercells 'L1$_2$-like' and 'D0$_{22}$-like' to study the crystal structure of $Ni_3Al_{0.75}Ta_{0.25}$ (atomic ratio is 12:3:1). Both these supercells consist of four $L1_2$ subcells with total 16 atoms. Fig. 10a shows the $L1_2$-like structure and the view from the direction [010]. This supercell can be created from a supercell containing four $L1_2$ Ni_3Al subcells, but the Al at the face centers shared by these four subcells, are replaced by Ta. Since there are six Ni at the face centers in each subcell (three Ni atoms), altogether there are twelve Ni atoms in the $L1_2$-like supercell. In addition, there are six Al (6/8 Al atom) and two Ta (2/8 Ta atom) occupying the corners in each subcell, so the total number of atoms for Al and Ta is three and one, respectively. Therefore, in the supercell the atomic ratio is 12:3:1. The $D0_{22}$-like supercell (Fig. 10b) is similar to the $L1_2$-like supercell and possesses the same atomic ratio of 12:3:1. The difference between these two supercells is that the Ta in $D0_{22}$-like supercell is at the body center (occupy Ni sites) instead of being at the middle corners (occupy Al sites) in $L1_2$-like supercell.

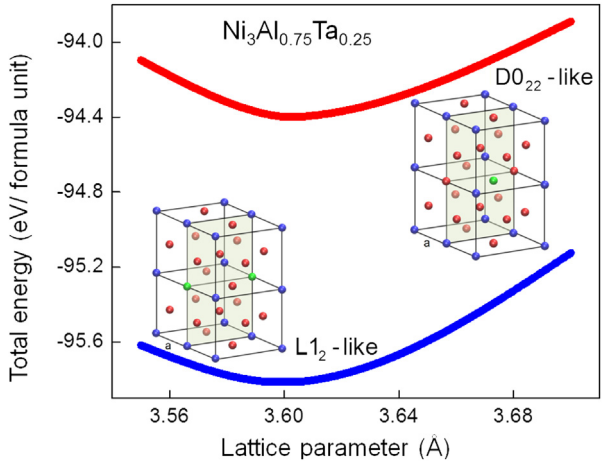

Fig. 11. Total energy as a function of lattice parameter for $Ni_3Al_{0.75}Ta_{0.25}$ $D0_{22}$-like structure (read line) and $L1_2$-like structure (blue line). The total energies of the $L1_2$-like structure are lower than those of the $D0_{22}$-like structure by near 1.2 eV per formula unit. The calculated lattice parameter is compared to other calculations and experiments shown in Table 1. (For interpretation of the references to color in this figure legend, the reader is referred to the web version of this article.)

We calculated total energy as a function of lattice parameter of $D0_{22}$-like and $L1_2$-like to determine the stability of these two different structures in $Ni_3Al_{0.75}Ta_{0.25}$ (Fig. 11). Similar to the case of $Ni_3Al_{0.5}Ta_{0.5}$, $Ni_3Al_{0.75}Ta_{0.25}$ in the $L1_2$-like structure has lower total energies than those of the $D0_{22}$-like structure by near 1.2 eV per formula unit. Thus, $Ni_3Al_{0.75}Ta_{0.25}$ in the $L1_2$-like structure is energetically favored over the one in the $D0_{22}$-like structure. These results are expected when we consider the $Ni_3Al_{0.75}Ta_{0.25}$ as the ternary additions of Ta in Ni_3Al, the Ta will preferentially occupy the Al sites ($L1_2$-like structure) over than the Ni sites ($D0_{22}$-like structure) [61,63,71]. Therefore, in the

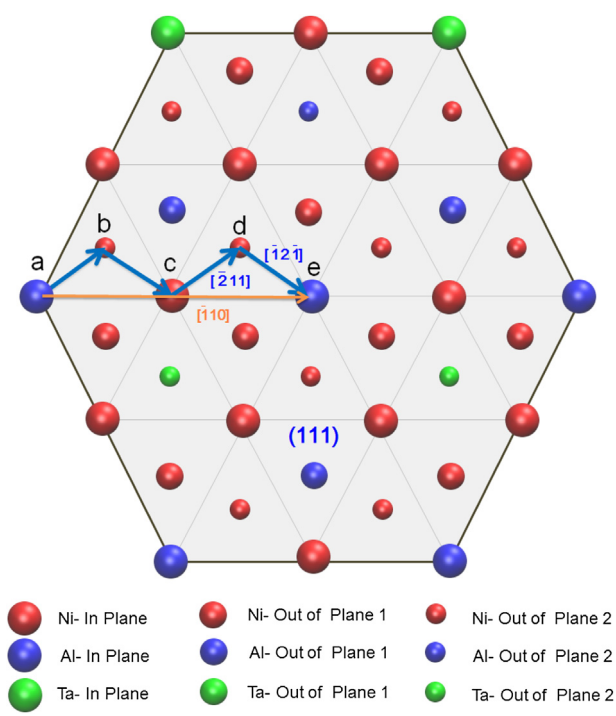

Fig. 12. Dislocations and atomic configuration of $L1_2$-like $Ni_3Al_{0.75}Ta_{0.25}$ in the (111) plane. Three different sizes of atoms represent three successive (111) layers from the top view. Dislocation $[\bar{1}10]$ can dissociate into four superpartials 1/6<2 1 1> corresponding to Eq. (1). Two types of planar defects CSF (a → b and c → d) and APB (a → c and c → e) are formed. The points a, b, c, d and e correspond to the stable (metastable) positions of GSFE curve described later.

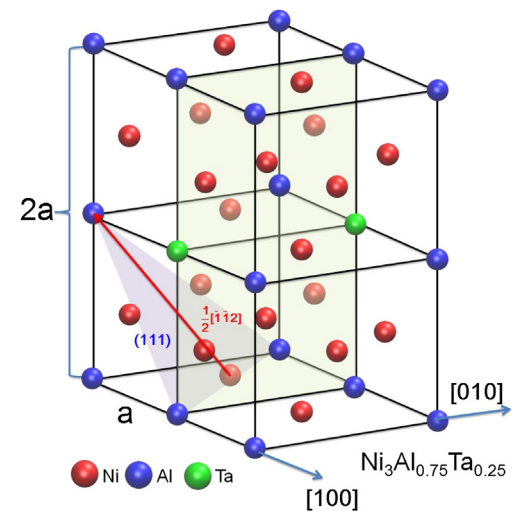

Fig. 13. Slip plane (111) (shaded violet) and slip direction $\left[\bar{1}\,\bar{1}2\right]$ (red arrow) in $L1_2$-like $Ni_3Al_{0.75}Ta_{0.25}$. The $L1_2$-like supercell consists of four $L1_2$ subcells with total 16 atoms. (For interpretation of the references to color in this figure legend, the reader is referred to the web version of this article.)

following studies of dislocation slip and twin nucleation in $Ni_3Al_{0.75}Ta_{0.25}$, we established the GSFE and GPFE curves for $L1_2$-like structure as it is more energetically stable.

3.2.2. Dislocation slip (GSFE) in $L1_2$-like $Ni_3Al_{0.75}Ta_{0.25}$

Similar to the dislocation slip in $Ni_3Al_{0.5}Ta_{0.5}$, the slip system {111}<110> is considered to study the dislocation slip in $Ni_3Al_{0.75}Ta_{0.25}$. Fig. 12 shows the superdislocation <110> in the {111} slip plane dissociated into four superpartials 1/6<211> with formation of CSF and APB energies (see Eq. (1)).

Fig. 13 shows the unit cell of $L1_2$-like $Ni_3Al_{0.75}Ta_{0.25}$ with the slip plane (111) (shaded violet) and slip direction $[\bar{1}\,\bar{1}2]$ (red arrow). The lattice parameter a is calculated as 3.60 Å in Fig. 11, which is in a good agreement with experimental measurements (Table 1).

The slip system $1/6\left[\bar{1}\,\bar{1}2\right](111)$ of $L1_2$-like $Ni_3Al_{0.75}Ta_{0.25}$ is illustrated in Fig. 14 with the slip plane (111) and dislocation $1/6\left[\bar{1}\,\bar{1}2\right]$. Fig. 14a is the perfect $L1_2$-like lattice before shear, while Fig. 14b is the lattice after shear by one Burgers vector, $b = \sqrt{6}/6a = 1.47$Å, in the slip plane.

We calculated the GSFE curve in the slip system 1/6<112>(111) of $L1_2$-like $Ni_3Al_{0.75}Ta_{0.25}$ shown in Fig. 15. The points a, b, c, d and e correspond to the stable (metastable) positions in the GSFE curve (see atomic configuration in Fig. 12). The calculated stacking fault energies are compared well to other calculations and experimental data in Table 2. The Peierls stress of $L1_2$-like $Ni_3Al_{0.75}Ta_{0.25}$ is calculated as 517 MPa in Table 2.

3.2.3. Twin nucleation (GPFE) in $L1_2$-like $Ni_3Al_{0.75}Ta_{0.25}$

We calculated the GPFE curve of $L1_2$-like $Ni_3Al_{0.75}Ta_{0.25}$ by successive shear of every (111) plane over $1/6\left[\bar{1}\,\bar{1}2\right]$ twinning partial (the twinning Burgers vector $b = \sqrt{6}/6a = 1.47$ A). Fig. 16a shows the perfect lattice of $L1_2$-like $Ni_3Al_{0.75}Ta_{0.25}$, while Fig. 16b is the lattice with a three-layer twin after shearing 3b (shown in a red arrow) in successive (111) planes (twin plane is marked with a brown dashed line). The atomic arrangement is viewed from the $[\bar{1}10]$ direction.

The calculated energy landscape (GPFE) for a three-layer twin formation in $L1_2$-like $Ni_3Al_{0.75}Ta_{0.25}$ is shown in Fig. 17. The calculated energies associated to the twin process, and the critical twin nucleation stress of 395 MPa are shown in Table 2.

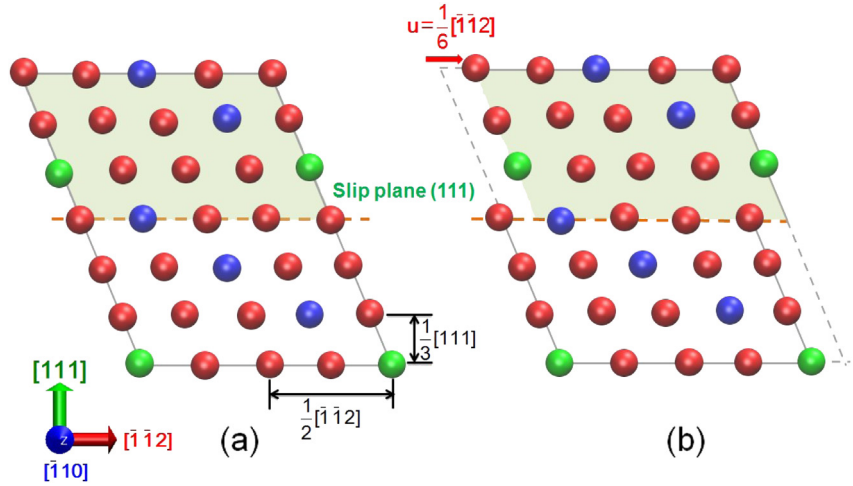

Fig. 14. Dislocation slip in the (111) plane with dislocation $1/6[\bar{1}\,\bar{1}2]$ of $L1_2$-like $Ni_3Al_{0.75}Ta_{0.25}$. (a) The perfect $L1_2$-like lattice observed from the $[\bar{1}10]$ direction. The slip plane (111) is marked with a brown dashed line. (b) The lattice after a rigid shear with dislocation $1/6[\bar{1}\,\bar{1}2]$, u, shown in a red arrow. (For interpretation of the references to color in this figure legend, the reader is referred to the web version of this article.)

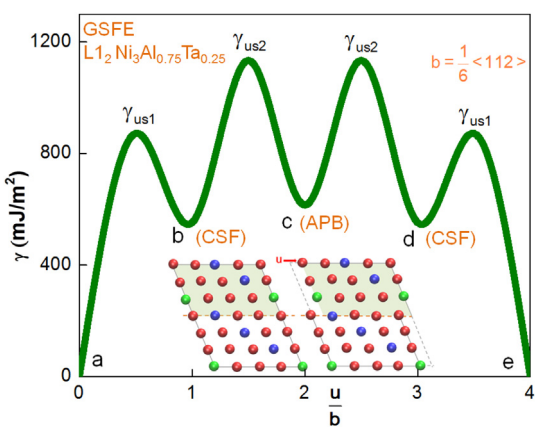

Fig. 15. The GSFE curve of the slip system $1/6\langle 112\rangle(111)$ in $L1_2$-like $Ni_3Al_{0.75}Ta_{0.25}$. The dislocation $[\bar{1}10]$ can dissociate into four superpartials $1/6\langle 112\rangle$ connected by stacking fault energies CSF and APB. The calculated stacking fault energies are shown in Table 2. The points a, b, c, d and e correspond to the stable (metastable) positions in the GSFE curve (see atomic configuration in Fig. 12).

4. Conclusions

In this study, we predicted the dislocation slip and twinning stresses for Ni_3 (Al, Ti, Ta, Hf) compositions with $L1_2$ crystal structures based on the extended Peierls–Nabarro model for slip and the proposed twin nucleation model. These models provide quantitative understanding and guidelines for selecting optimal precipitate chemistry and composition to obtain higher mechanical strength in SMAs. The calculated results support the following conclusions:

(1) The twinning stress for the intermetallic Ni_3 (Al, Ta) and Ni_3 (Al, Hf) compositions were found to be lower compared to the slip stress.
(2) The increase in flow stress with increasing Ta and Hf contents in Ni_3Al is substantial. With addition of Ta (in the range $x = 0$ to 0.5 for $Ni_3Al_{(1-x)}Ta_x$) the slip stress increased from 164 MPa to 603 MPa and the twinning stress from 148 MPa to 490 MPa, respectively. For the case of Hf addition, the increase in stress levels was more significant; they were as high 588 MPa and 456 MPa for slip and twinning respectively corresponding to the $x = 0.25$ for $Ni_3Al_{(1-x)}Hf_x$ case.
(3) Internal relaxation of atoms was allowed in obtaining the energy landscapes for slip-GSFE and for twinning-GPFE. Both the twin and slip planes were (111) and the Burgers vector

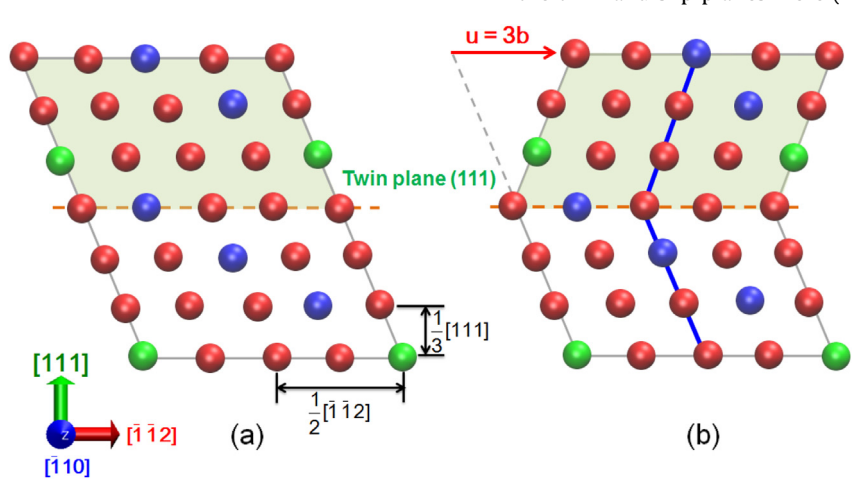

Fig. 16. (a) The perfect $L1_2$-like lattice viewed from the $[\bar{1}10]$ direction. Twin plane (111) is marked with a brown dashed line. (b) The lattice with a three-layer twin after shearing 3b along $1/6\left[\bar{1}\,\bar{1}2\right]$ shown in a red arrow. (For interpretation of the references to color in this figure legend, the reader is referred to the web version of this article.)

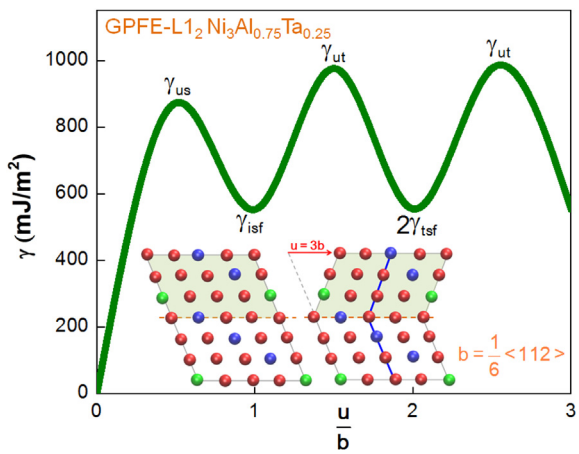

Fig. 17. The GPFE curve in the twin plane (111) with the twin dislocation $b = 1/6\left[\bar{1}\,\bar{1}2\right]$ of $L1_2$-like $Ni_3Al_{0.75}Ta_{0.25}$. The shear displacement, u, is normalized by the twinning Burgers vector $b = 1/6\left[\bar{1}\,\bar{1}2\right]$. The calculated fault energies are shown in Table 2.

was <112> type. The theoretical APB (anti-phase boundary) energy and CSF (complex stacking fault) energy values matched the experiments.

(4) The predicted flow stress values are in general agreement with experiments for the cases where experimental data is available. There appears to be considerable scatter in experimental values; however, the theory captures the trends accurately.

Acknowledgments

The support of the work by National Science Foundation, CMMI 13-33884, is gratefully acknowledged.

Appendix A. Prediction of Peierls stress for dislocation slip by extended P–N model

To calculate the Peierls stress, τ_p, for dislocation slip, a potential energy of displacement associated with the dislocation movement, misfit energy $E_\gamma(u)$, was determined [72,73]. This energy depends on the position of the dislocation line within a lattice cell and reflects the lattice periodicity, thus it is periodic [74,75]. The $E_\gamma(u)$ is defined as the sum of misfit energies between pairs of atomic planes and is calculated from the GSFE at the local disregistry [31]:

$$E_\gamma(u) = \sum_{m=-\infty}^{+\infty} \gamma[f(ma' - u)]a' \tag{A.1}$$

where, $\gamma[f(x)]$ is determined from GSFE curve, a' is the periodicity of E_γ and defined as the shortest distance between two equivalent atomic rows in the direction of the dislocation displacement, $f(x)$ is the disregistry function representing the relative displacement of the two half crystals in the slip plane along the x direction [3,5,76] and u is the position of dislocation line.

The disregistry function $f(x)$ can be described in Eq. (A2) by considering the multiple partials:

$$f(x) = \frac{b}{\pi}\left[\arctan\left(\frac{x}{\zeta}\right) + \arctan\left(\frac{x - d_C}{\zeta}\right) + \arctan\left(\frac{x - (d_C + d_A)}{\zeta}\right) + \arctan\left(\frac{x - (2d_C + d_A)}{\zeta}\right)\right] + 2b \tag{A.2}$$

Fig. A.1 shows the normalized $f(x)/b$ variation with x/ζ in $L1_2$-like $Ni_3Al_{0.75}Ta_{0.25}$, where ζ is the half width of the dislocation core. The separation distances, $d_C = 11.4$ Å and $d_A = 14.9$ Å, of partial dislocations are calculated using the force balance between attraction due to fault energies and elastic repulsion of partial dislocations [77–79].

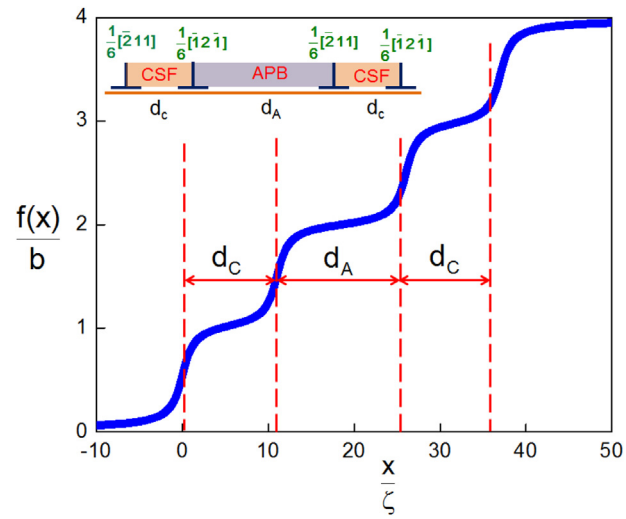

Fig. A.1. The disregistry function $f(x)$ for the superdislocation $[\bar{1}10]$ dissociated into four partials 1/6<211> in $L1_2$-like $Ni_3Al_{0.75}Ta_{0.25}$. The separation distances of the partial dislocations are calculated as $d_C = 11.4$ Å and $d_A = 14.9$ Å.

After determining the $f(x)$ and approximating the GSFE curve by a sinusoidal series function (Fig. 15), we can calculate the misfit energy in Eq. (A.1). Fig. A.2 shows the misfit energy $E_\gamma(u)$ variation with the lattice period a' for the superdislocation $[\bar{1}10]$ of $Ni_3Al_{0.75}Ta_{0.25}$. Therefore, the Peierls stress τ_p can be calculated by the maximum of $(1/b)(dE^s_\gamma(u)/du)$. Two quantities $(E^s_\gamma)_{a'/2}$ and $(E^s_\gamma)_p$ in the plot are denoted. The $(E^s_\gamma)_{a'/2}$ represents the minimum of $E^s_\gamma(u)$ function and provides an estimate of the core energy of dislocations. The $(E^s_\gamma)_p$ is defined as the Peierls energy, which is the amplitude of the variation of $E^s_\gamma(u)$ and the barrier required to move dislocations [75,11].

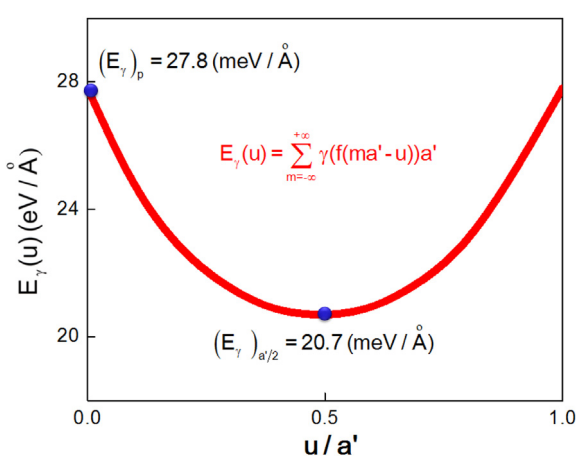

Fig. A.2. Misfit energy $E_\gamma(u)$ for the superdislocation $[\bar{1}10]$ of $Ni_3Al_{0.75}Ta_{0.25}$.

Appendix B. Prediction of critical twin nucleation stress by twin nucleation model

We have developed a twin nucleation model to predict the critical twin nucleation stress in alloys (see details in Ref. [10]). In the present study, the twin nucleation stress for Ni-based alloys was predicted utilizing this model. We determined the total energy involved in the twin nucleation as follows:

$$E_{total} = E_{int} + E_{GPEE} + E_{line} - W = \frac{\mu b^2}{4\pi(1-\nu)}\left(1-\nu\cos^2\theta\right)\sum_{m=1}^{N-1}\left(\sum_{i=1}^{m}\ln\frac{L}{d_i}+\sum_{i=2}^{m}\ln\frac{L}{d_i}+\ldots+\sum_{i=N-1}^{m}\ln\frac{L}{d_i}\right)+\sum_{m=-\infty}^{+\infty}\gamma_{SF}[f(mb)]b$$
$$+(N-1)\sum_{m=-\infty}^{+\infty}\gamma_{twin}[f(mb)]b+\frac{N\mu b^2}{2(1-\nu)}\left(1-\nu\cos^2\theta\right)-\sum_{i=1}^{N-1}\tau shd_i,\quad i=1,2,3,\ldots,N-1, \tag{B.1}$$

where, E_{int} is the twin dislocations interaction energy, E_{GPEE} is the twin boundary energy (GPFE), E_{line} is the twin dislocations line energy and W is the applied work; μ is the shear modulus in the twinning system, b is the Burgers vector of the twinning dislocation, ν is the Poisson's ratio, θ is the angle between the Burgers vector and the dislocation line, L is the dimensions of the crystal containing the twin; τ is the applied shear stress and the minimum τ to form a twin is called critical twin nucleation stress, τ_{crit}; N is the number of twin nucleation layers, h is the twin thickness and d_i is the equilibrium spacing between two adjacent twinning dislocations i and $i+1$ corresponding to the minimum total energy. Fig. B.1 shows a schematic of twin formation in $Ni_3Al_{0.75}Ta_{0.25}$, where $N=3$ and $i=1,2$ are determined corresponding to Eq. (B.1). We note that depending on the crystal structure and twin system, the number of twin nucleation layers, N, can have values other than 3, so we keep N in the following equations for general cases.

$$f(x) = \frac{b}{2}+\frac{b}{N\pi}\left\{\tan^{-1}\left(\frac{x}{\zeta}\right)+\tan^{-1}\left(\frac{x-d_1}{\zeta}\right)+\ldots\right.$$
$$\left.+\tan^{-1}\left(\frac{x-d_1-d_2-\ldots-d_i}{\zeta}\right)\right\},\quad i=1,2,3,\ldots N-1, \tag{B.2}$$

To determine the critical stress, τ_{crit}, we minimized the total energy for the twin nucleation, E_{total}, with respect to d_i:

$$\frac{\partial E_{total}}{\partial d_i} = 0,\quad i=1,2,3,\ldots,N-1, \tag{B.3}$$

By numerically solving the above set of N − 1 equations, the critical twinning stress can be determined as the minimum value of the applied stress where these equations satisfy. We note that all parameters involved in the equations Eqs. (B1)–(B3) can be calculated from atomistic simulations, and no fitting parameter from experimental measurements is needed. Therefore, we

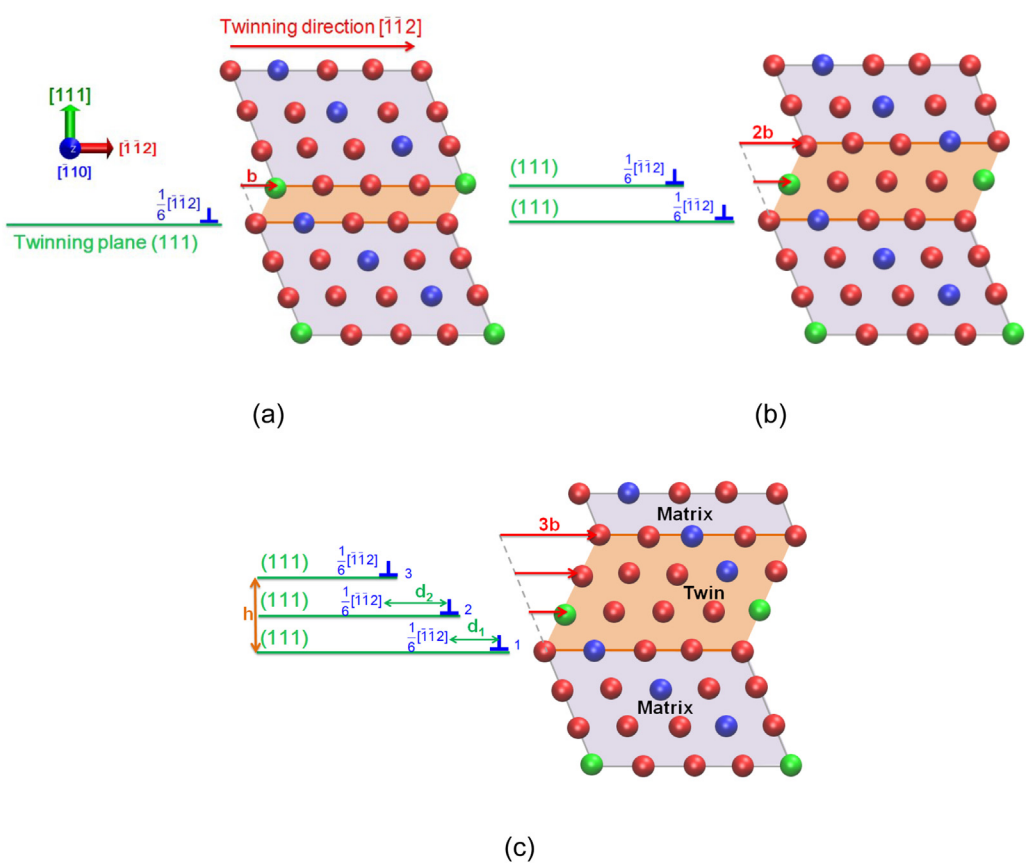

Fig. B.1. Schematic of twin formation in $Ni_3Al_{0.75}Ta_{0.25}$, where the twin layers result from the glide of (a) one, (b) two, (c) three twinning dislocations $b = 1/6[\bar{1}\bar{1}2]$ in the twinning plane (111). The left-hand side of these figures shows the glide sequence of $b = 1/6[\bar{1}\bar{1}2]$, and the right-hand side is the atomic arrangements of twin formation viewed from $[\bar{1}10]$ direction. $N=3$ is the number of twin-layers, h is the twin thickness and d_i is the equilibrium spacing between two adjacent twinning dislocations i and $i+1$ corresponding to the minimum total energy (i = 1, 2).

The disregistry function $f(x)$ considering the interaction of multiple twinning dislocations is derived as the following:

predict the twin nucleation stress for the Ni-based alloys in Table 2.

References

[1] Ogata S, Li J, Yip S. Twinning pathway in BCC molybdenum. Europhys Lett 2004;68:405.
[2] Schoeck G. The Peierls stress in a simple cubic lattice. Phys Status Solidi B 2011;248:2284–9.
[3] Carrez P, Ferré D, Cordier P. Peierls-Nabarro model for dislocations in $MgSiO_3$ post-perovskite calculated at 120 GPa from first principles. Philos Mag 2007;87:3229–47.
[4] Nabarro FRN. Theoretical and experimental estimates of the Peierls stress. Philos Mag A 1997;75:703–11.
[5] Joós B, Duesbery MS. The peierls stress of dislocations: an analytic formula. Phys Rev Lett 1997;78:266–9.
[6] Wang JN. Prediction of Peierls stresses for different crystals. Mater Sci Eng A 1996;206:259–69.
[7] Lu G, Kioussis N, Bulatov VV, Kaxiras E. The Peierls-Nabarro model revisited. Philos Mag Lett 2000;80:675–82.
[8] Kibey S, Liu JB, Johnson DD, Sehitoglu H. Predicting twinning stress in fcc metals: linking twin-energy pathways to twin nucleation. Acta Mater 2007;55:6843.
[9] Ogata S, Ju L, Yip S. Energy landscape of deformation twinning in bcc and fcc metals. Phys Rev B Condens Matter Mater Phys 2005;71:224102.
[10] Wang J, Sehitoglu H. Twinning stress in shape memory alloys: theory and experiments. Acta Mater 2013;61:6790–801.
[11] Wang J, Sehitoglu H, Maier HJ. Dislocation slip stress prediction in shape memory alloys. Int J Plast 2014:247–66.
[12] Ezaz T, Sehitoglu H, Maier HJ. Energetics of twinning in martensitic NiTi. Acta Mater 2011;59:5893–904.
[13] Kokorin VV, Martynov VV, Chernenko VA. Stress-induced martensitic transformations in Ni_2MnGa. Scr Metall Mater 1992;26:175–7.
[14] Soolshenko V, Lanska N, Ullakko K. Structure and twinning stress of martensites in non-stoichiometric Ni_2MnGa single crystal. In: International conference on martensitic transformations, June 10, 2002–June 14, 2002. Espoo, Finland: EDP Sciences; 2003. pp. 947–50.
[15] Appel F, Paul JDH, Oehring M. Gamma titanium aluminide alloys: science and technology. Wiley; 2011.
[16] Jost N. Thermal fatigue of Fe-Ni-Co-Ti shape-memory-alloys. Mater Sci Eng A 1999;273–275:649–53.
[17] Maki T, Kobayashi K, Minato M, Tamura I. Thermoelastic martensite in an ausaged Fe-Ni-Ti-Co alloy. Scr Metall 1984;18:1105–9.
[18] Jian L, Chou C, Wayman C. Martensitic transformation and the shape memory effect in an Fe-33Ni-12Co-5Ti alloy. Mater Chem Phys 1993;34:14–23.
[19] Ma J, Hornbuckle B, Karaman I, Thompson G, Luo Z, Chumlyakov Y. The effect of nanoprecipitates on the superelastic properties of FeNiCoAlTa shape memory alloy single crystals. Acta Mater 2013;61:3445–55.
[20] Sehitoglu H, Efstathiou C, Maier HJ, Chumlyakov Y. Hysteresis and deformation mechanisms of transforming FeNiCoTi. Mech Mater 2006;38:538.
[21] Tanaka Y, Himuro Y, Kainuma R, Sutou Y, Omori T, Ishida K. Ferrous polycrystalline shape-memory alloy showing huge superelasticity. Science 2010;327:1488–90.
[22] Hornbogen E. The effect of variables on martensitic transformation temperatures. Acta Metall 1985;33:595–601.
[23] Koval YN, Monastyrsky G. On the nature of the variation of martensitic transformation hysteresis and SME characteristics in Fe-Ni-base alloys. J Phys IV 1995;5. C8-397-C398-402.
[24] Ma J, Kockar B, Evirgen A, Karaman I, Luo Z, Chumlyakov Y. Shape memory behavior and tension-compression asymmetry of a FeNiCoAlTa single-crystalline shape memory alloy. Acta Mater 2012;60:2186–95.
[25] Vitek V. Intrinsic stacking faults in body-centred cubic crystals. Philos Mag 1968;18:773.
[26] Kibey SA. Mesoscale models for stacking faults, deformation twins and martensitic transformations: linking atomistics to continuum. ProQuest; 2007.
[27] Kresse G, Hafner J. Ab initio molecular dynamics for open-shell transition metals. Phys Rev B Condens Matter 1993;48:13115.
[28] Kresse G, Furthmuller J. Efficient iterative schemes for ab initio total-energy calculations using a plane-wave basis set. Phys Rev B Condens Matter 1996;54:11169.
[29] Fu CL, Yoo MH. Deformation behavior of B2 type aluminides: FeAl and NiAl. Acta Metall Mater 1992;40:703–11.
[30] Paidar V. Generalized stacking faults in model lattice of ordered Fe-Si alloys. Czechoslov J Phys 1976;26:865–74.
[31] Juan Y-M, Kaxiras E. Generalized stacking fault energy surfaces and dislocation properties of silicon: a first-principles theoretical study. Philos Mag A 1996;74:1367–84.
[32] Xie H-X, Bo L, Yu T. Atomistic simulation of microtwinning at the crack tip in L12 Ni_3Al. Philos Mag 2012;92:1542–53.
[33] Xie H-X, Wang C-Y, Yu T, Du J-P. Condensed matter: structure, thermal and mechanical properties: dislocation formation and twinning from the crack tip in Ni_3Al: molecular dynamics simulations. Chin Phys B 2009;18:251–8.
[34] Voskoboinikov R, Rae C. A new γ-surface in {111} plane in L12 Ni_3Al. In: IOP conference series: materials science and engineering. IOP Publishing; 2009. p. 012009.
[35] Mryasov ON, Gornostyrev YN, van Schilfgaarde M, Freeman AJ. Superdislocation core structure in $L1_2$ Ni_3Al, Ni_3Ge and Fe_3Ge: Peierls-Nabarro analysis starting from ab-initio GSF energetics calculations. Acta Mater 2002;50:4545–54.
[36] Chou C, Hirsch P. Computer simulation of the motion of screw dislocations in Ni_3Al. Philos Mag A 1993;68:1097–128.
[37] Veyssiere P, Douin J, Beauchamp P. On the presence of super lattice intrinsic stacking faults in plastically deformed Ni_3Al. Philos Mag A 1985;51:469–83.
[38] Kim DE, Shang SL, Liu ZK. Effects of alloying elements on elastic properties of Ni_3Al by first-principles calculations. Intermetallics 2010;18:1163–71.
[39] Sun J, Lee C, Lai J, Wu J. Dislocation dissociations and fault energies in Ni_3Al alloys doped with palladium. Intermetallics 1999;7:1329–35.
[40] Wang Y-J, Gao G-JJ, Ogata S. Size-dependent transition of deformation mechanism, and nonlinear elasticity in Ni_3Al nanowires. Appl Phys Lett 2013;102:041902–5.
[41] Viswanathan G, Karthikeyan S, Sarosi P, Unocic R, Mills M. Microtwinning during intermediate temperature creep of polycrystalline Ni-based superalloys: mechanisms and modelling. Philos Mag 2006;86:4823–40.
[42] Kovarik L, Unocic R, Li J, Sarosi P, Shen C, Wang Y, et al. Microtwinning and other shearing mechanisms at intermediate temperatures in Ni-based superalloys. Prog Mater Sci 2009;54:839–73.
[43] Tichelaar F, Rongen P, Zhang Y, Schapink F. Slip transfer at coherent twin boundaries in Ni_3Al and ordered Cu_3Au. Interface Sci 1994;2:105–17.
[44] Wu J, Wen L, Tang B-Y, Peng L-M, Ding W-J. Generalized planner fault energies, twinning and ductility of $L1_2$ type Al_3Sc and Al_3Mg. Solid State Sci 2011;13:120–5.
[45] Umakoshi Y, Pope D, Vitek V. The asymmetry of the flow stress in Ni_3(Al, Ta) single crystals. Acta Metall 1984;32:449–56.
[46] Ezz S, Hirsch P. The strain rate sensitivity of the flow stress and the mechanism of deformation of single crystals of Ni_3(Al Hf)B. Philos Mag A 1994;69:105–27.
[47] Oblak J, Owczarski W, Kear B. Heterogeneous precipitation of metastable γ'-ni_3ti in a nickel base alloy. Acta Metall 1971;19:355–63.
[48] Baldan A. An investigation of the mechanism of thermally activated deformation in certain Ni-Al-Ta and Ni-Al-Hf superalloys. Phys Status Solidi A 1984;83:507–11.
[49] Stoloff N. Physical and mechanical metallurgy of Ni_3Al and its alloys. Int Mater Rev 1989;34:153–84.
[50] Holdway P, Staton-Bevan A. Dislocation structures in Zr_3Al-based alloys. J Mater Sci 1986;21:2843–9.
[51] Rao PM, Suryanarayana S, Murthy KS, Naidu SN. The high-temperature thermal expansion of Ni_3Al measured by X-ray diffraction and dilation methods. J Phys Condens Matter 1989;1:5357.
[52] Westbrook J, Fleischer R, Yoo M. Intermetallic compounds: principles and practice, vols. 1 and 2. MRS Bull Mater Res Soc 1997;22:51–2.
[53] Mishima Y, Ochiai S, Suzuki T. Lattice parameters of Ni (γ), Ni_3Al (γ') and Ni_3Ga (γ') solid solutions with additions of transition and B-subgroup elements. Acta Metall 1985;33:1161–9.
[54] Kuznetsov V. Aluminium-nickel-tantalum.
[55] Zhang Z, Huang X, Zhang ZX. Hexagonal metastable phase formation in Ni_3RM (RM = Mo, Nb, Ta) multilayered films by solid-state reaction. Acta Mater 1998;46:4189–94.
[56] Kruml T, Conforto E, Lo Piccolo B, Caillard D, Martin J. From dislocation cores to strength and work-hardening: a study of binary Ni_3Al. Acta Mater 2002;50:5091–101.
[57] Cui C, Demura M, Kishida K, Hirano T. Ductility of cold-rolled and recrystallized Ni_3Al foils. J Mater Res 2005;20:1054–62.
[58] Yoo M, Fu C, Horton J. Crack-tip dislocations and fracture behavior in Ni_3Al and Ni_3Si. Mater Sci Eng A 1994;176:431–7.
[59] Chandran M, Sondhi S. First-principle calculation of APB energy in Ni-based binary and ternary alloys. Model Simul Mater Sci Eng 2011;19:025008.
[60] Vamsi K, Karthikeyan S. Effect of off-stoichiometry and ternary additions on planar fault energies in Ni_3Al. Superalloys; 2012:521–30.
[61] Xu J-H, Oguchi T, Freeman A. Solid-solution strengthening: substitution of V in Ni_3Al and structural stability of Ni_3(Al, V). Phys Rev B 1987;36:4186.
[62] Colinet C, Pasturel A. Ab initio calculation of the formation energies of $L1_2$, $D0_{22}$, $D0_{23}$ and one dimensional long period structures in $TiAl_3$ compound. Intermetallics 2002;10:751–64.
[63] Ravindran P, Subramoniam G, Asokamani R. Ground-state properties and relative stability between the $L1_2$ and DO_a phases of Ni_3Al by Nb substitution. Phys Rev B 1996;53:1129.
[64] Maurer R. In situ straining: crack development in thin foils of Ni_3Al. J Mater Sci 1992;27:6279–90.
[65] Paidar V, Yamaguchi M, Pope D, Vitek V. Dissociation and core structure of $\langle 110 \rangle$ screw dislocations in L12 ordered alloys II. Effects of an applied shear stress. Philos Mag A 1982;45:883–94.
[66] Sun Y, Beltz GE, Rice JR. Estimates from atomic models of tension-shear coupling in dislocation nucleation from a crack tip. Mater Sci Eng A 1993;170:67–85.
[67] Suzuki K, Ichihara M, Takeuchi S. Dissociated structure of superlattice dislocations in Ni_3Ga with the L12 structure. Acta Metall 1979;27:193–200.

[68] Schoeck G, Kohlhammer S, Fahnle M. Planar dissociations and recombination energy of [110] superdislocations in Ni_3Al: generalized Peierls model in combination with ab initio electron theory. Philos Mag Lett 1999;79:849–57.
[69] Müllner P, King A. Deformation of hierarchically twinned martensite. Acta Mater 2010;58:5242–61.
[70] Romanov AE, Kolesnikova AL. Application of disclination concept to solid structures. Prog Mater Sci 2009;54:740–69.
[71] Lin H, Pope DP. The location of tantalum atoms in Ni_3Al. In: MRS proceedings. Cambridge Univ Press; 1988.
[72] Tadmor EB, Miller RE. Modeling materials: continuum, atomistic and multiscale techniques. Cambridge University Press; 2011.
[73] Nabarro FRN. Dislocation in a simple cubic lattice. Proc Phys Soc 1947;59.
[74] Schoeck G. Peierls energy of dislocations: a critical assessment. Phys Rev Lett 1999;82:2310–3.
[75] Joós B, Ren Q, Duesbery MS. Peierls-Nabarro model of dislocations in silicon with generalized stacking-fault restoring forces. Phys Rev B 1994;50:5890–8.
[76] Lejček L. On minimum of energy in the Peierls-Nabarro dislocation model. Czechoslov J Phys 1973;23:176–8.
[77] Stroh AN. Dislocations and cracks in anisotropic elasticity. Philos Mag 1958;3:625–46.
[78] Crawford RC, Ray ILF, Cockayne DJH. The weak-beam technique applied to superlattice dislocations in iron-aluminium alloys. Philos Mag 1973;27:1–7.
[79] Sehitoglu H, Wang J, Maier HJ. Transformation and slip behavior of Ni_2FeGa. Int J Plast 2012;39:61–74.